



This open access document is posted as a preprint in the Beilstein Archives at <https://doi.org/10.3762/bxiv.2023.38.v1> and is considered to be an early communication for feedback before peer review. Before citing this document, please check if a final, peer-reviewed version has been published.

This document is not formatted, has not undergone copyediting or typesetting, and may contain errors, unsubstantiated scientific claims or preliminary data.

**Preprint Title**  $\text{Ti}_3\text{C}_2\text{T}_x$  MXene as a surface-enhanced Raman scattering substrate

**Authors** Hayk Minassian, Armen Melikyan, Manuel R. Goncalves and Petros Petrosyan

**Publication Date** 11 Sep. 2023

**Article Type** Full Research Paper

**Supporting Information File 1** Final SI\_revised\_MRG\_v3.pdf; 730.3 KB

**ORCID® IDs** Hayk Minassian - <https://orcid.org/0000-0002-5802-0210>; Manuel R. Goncalves - <https://orcid.org/0000-0001-9050-7857>; Petros Petrosyan - <https://orcid.org/0000-0002-8611-5479>



License and Terms: This document is copyright 2023 the Author(s); licensee Beilstein-Institut.

This is an open access work under the terms of the Creative Commons Attribution License (<https://creativecommons.org/licenses/by/4.0>). Please note that the reuse, redistribution and reproduction in particular requires that the author(s) and source are credited and that individual graphics may be subject to special legal provisions.

The license is subject to the Beilstein Archives terms and conditions: <https://www.beilstein-archives.org/xiv/terms>.

The definitive version of this work can be found at <https://doi.org/10.3762/bxiv.2023.38.v1>

## **Ti<sub>3</sub>C<sub>2</sub>T<sub>x</sub> MXene as a surface-enhanced Raman scattering substrate**

**Hayk Minassian<sup>1</sup>, Armen Melikyan<sup>2</sup>, Manuel Rodrigues Goncalves<sup>\*3</sup> and Petros Petrosyan<sup>4</sup>**

Address: <sup>1</sup>A. Alikhanian National Science Laboratory, Alikhanyan Str. Build. 2, 0036, Yerevan, Armenia; <sup>2</sup>Institute of Applied Problems of Physics of NAS, 25, Hr. Nersessian Str., 0014, Yerevan, Armenia; <sup>3</sup>Ulm University, Institute of Experimental Physics, Albert-Einstein-Allee 11, 89081 Ulm, Germany and <sup>4</sup>Yerevan State University, 1 Alek Manukyan Str., 0025, Yerevan, Armenia.

E-mail: Hayk Minassian - [hminassian@yerphi.am](mailto:hminassian@yerphi.am);

Manuel Rodrigues Goncalves - [manuel.goncalves@uni-ulm.de](mailto:manuel.goncalves@uni-ulm.de);

\* Correspondence: [manuel.goncalves@uni-ulm.de](mailto:manuel.goncalves@uni-ulm.de), [hminassian@yerphi.am](mailto:hminassian@yerphi.am)

### **Abstract**

Surface-enhanced Raman scattering (SERS) of R6G molecule near Ti<sub>3</sub>C<sub>2</sub>T<sub>x</sub> MXene flakes is analyzed theoretically. The flakes are modeled as nanoparticles of different shape and size. In order to determine the enhancement factor (EF) of SERS the dye molecule is modeled as a small sphere with polarizability spectrum based on experimental data. In the wavelength range 500nm – 1000nm the main contribution to SERS in the case of MXene substrate comes from polarization

induced by two mechanisms - interband transitions (IBT), longitudinal quadrupole and transversal quadrupole surface plasmon (LQSP and TQSP) resonances. We show that both polarization mechanisms present low sensitivity to the shape and size of MXene flakes, which makes it advantageous to use these 2D materials for manufacturing of SERS substrates. The electromagnetic SERS enhancement is determined by the “lightning rod” and “hot-spot” effects due to partial overlapping of absorption spectrum of the R6G molecule with these MXene resonances. Good agreement between the calculated values of the EF and experimental data of  $Ti_3C_2T_x$  substrate is reached.

**Keywords:** MXene, SERS, surface plasmons, enhancement factor, absorption cross-section.

## Introduction

Around a decade ago, a new family of 2D materials has been discovered - carbides and nitrides of transition metals, called MXenes [1-2]. They are generically identified by  $M_{n+1}X_nT_x$ , where M stands for transition metal, X is either carbon or nitrogen,  $n = 1,2,3$  and  $T_x$  stands for termination species. The investigation of optical properties of MXenes has been carried out by electron energy loss spectroscopy (EELS) and optical measurements in the visible, UV, and IR ranges [3-6]. The analysis of experimental data allowed identifying bulk plasmons, surface plasmons (SPs) as well as IBT in these 2D metal carbides and nitrides [7]. Due to their unique optoelectronic properties as well as metal-like electronic conductivity, MXenes became the subject of intensive research [8]. The reason for this interest lies in the possible applications of MXenes as supercapacitors [9, 10], in optical sensing and light detection [11], in communication and

biology [12], in femtosecond mode-locked lasers [13], nanomaterial-based saturable absorbers for photonic devices [14], broadband optical filters [15], etc. These new 2D materials are also interesting for plasmonics at NIR wavelengths [5,16]. In [17], the optical properties of the most studied  $Ti_3C_2T_x$  MXene nanosheets were theoretically analyzed and the absorption cross-sections (ACS) were calculated. Particularly, it was shown that in the visible-NIR spectral range, along with the IBT and the transversal dipole surface plasmons (TDSP) already identified [5], there is a new resonance in the absorption spectra of  $Ti_3C_2T_x$ , caused by LQSP. The results of calculations were compared with known experimental data of EELS and optical absorption in visible range [3-5,15,18], and good agreement was found.

The exploitation of optical properties of MXenes is not limited to the possibility of creating new photonics devices. Another possible and important application is in SERS. MXenes are attractive candidates as SERS substrates because of their metallic conductivity and abundant surface terminations. The first experimental result for the EF of SERS from rhodamine 6G (R6G) on  $Ti_3C_2T_x$  deposited on glass and in aqueous solution was reported in [18]. In this study of 2017, using the dielectric function of  $Ti_3C_2T_x$  measured in [5], it was confirmed theoretically that SERS for incident light wavelengths between  $\lambda = 500nm$  to  $800nm$  is caused by IBT. The experimental data of EF, achieved values of the order of  $10^5 - 10^6$ . In [19], the SERS activity of the few layers of  $Ti_2NT_x$  was detected by fabricating a paper-based MXene substrate. Although the absorption spectrum of the MXene did not contain dipole surface plasmon peaks, an EF of  $10^{12}$  was reported for R6G molecules. SERS of rhodamine B molecules on a freestanding  $Ti_3C_2T_x$  membrane was investigated in [20] and a homogeneity of the MXene substrate was demonstrated. More recently, measurements revealed the possibility of exploiting  $Ti_3C_2T_x$ / AuNRs hybrids as a SERS platform for the thiram molecule detection [21]. It was shown in [22], that Raman spectra of  $Ti_3C_2T_x$  affected

by intercalated species and stacking and differences in Raman spectra collected from single flakes of  $Ti_3C_2T_x$ , colloidal solutions, and multilayer films were reported. In [23], highly crystalline monolayers of  $Ti_3C_2$  were synthesized by chemical exfoliation and microwave heating method. The corresponding EF of SERS signal of R6G was  $3.8 \times 10^8$ . It was explained by the authors as a result of dual effects: strong localized SPs and remarkable interfacial-charge-transfer. In [24], SERS from salicylic acid adsorbed on  $Ti_3C_2T_x$  film was observed. In [25] was shown, that  $Nb_2C$  and  $Ta_2C$  MXenes exhibit a SERS EF values of order of  $3 \times 10^6$  and  $1.4 \times 10^6$ , under excitation wavelength of 532nm. Recently in [26], different MXenes -  $Mo_2C$ ,  $Ti_2C$ ,  $V_2C$ ,  $Mo_2TiC_2$ , and  $Ti_3CN$  were synthesized as pristine substrates for SERS applications and in all MXenes a concentration of  $10^{-7}$  of R6G could be detected. In [27], other MXene – a  $TiVC$  film was used as SERS substrate. In this case a large EF was dominated by the chemical mechanism. In the Supporting Information (SI-Table 1) the available experimental data of EFs for different MXenes and the corresponding excitation wavelengths are presented.

We mention that sensitive detection of SERS under low molecular concentration is still far from satisfaction [28]. Regardless the large number of articles on experimental SERS measurements based on MXene substrates, to our knowledge the dominant mechanisms leading to the electromagnetic enhancement of the Raman signal are not revealed theoretically yet.

It is well known, that several electromagnetic mechanisms cause Raman scattering enhancement due to metallic nanoparticles (NP) either on the substrate, or in solution: a) the resonant excitation of SP [29], b) the image dipole enhancement effect [30], c) the increase of local field due to the strong curvature of the NP surface ("lightning rod" effect) [31], d) the "hot spot" effect [32, 33], etc. As the experiments and the corresponding calculations show, in the vis-NIR wavelength spectral range, commonly used in the SERS excitation and detection there are

no dipole SP resonances in the MXene spectra [3-5,15,18]. For example, in  $Ti_3C_2T_x$ , the real part of the dielectric function  $\epsilon(\omega)$  becomes negative only for wavelengths  $\lambda \geq 1130\text{nm}$  indicated in the onset of TDSPs [5]. By other side, EELS measurements based on  $Ti_3C_2T_x$  with different functional groups [3] and optical absorption measurements [18] exhibit maxima in the wavelength range  $\lambda = 500 - 1000\text{nm}$  which are responsible for SERS enhancement.

In this article, we discuss theoretically the SERS process of R6G molecules near  $Ti_3C_2T_x$  MXene substrates, using experimental data of the dielectric function. The simulations were performed using COMSOL Multiphysics software. The MXene NPs were modeled using different shapes and longitudinal sizes. In the spectral range of  $\lambda = 500 - 1000\text{nm}$ , it allowed us to identify contributions of IBT and quadrupole SP resonances, which could be responsible for SERS effect. Taken in account that synthesized  $Ti_3C_2T_x$  MXene samples investigated in experiments as SERS substrates have lateral dimensions in the micrometer range, we studied NPs of linear sizes up to  $2\mu\text{m}$ . For the optimization of EF, we also consider the contribution of the wavelength dependent absorption of the R6G dye molecule to the SERS effect. The absorption spectrum of R6G was measured in [34-36].

## Results and discussion

### 1. Isolated $Ti_3C_2T_x$ flake as SERS substrate

The calculation of the SERS EF for a probe dye molecule near MXene NPs of a various shapes and sizes, under illumination of a time-harmonic electromagnetic field, is based on the local field found by a numerical simulation. The theoretical EF,  $G$ , is defined according to the following expression:

$$G = \frac{|\vec{E}_{\text{total}}(\vec{r}_0, \omega)|^4}{|\vec{E}_0(\vec{r}_0, \omega)|^4} \quad (1)$$

$\vec{E}_{\text{total}}(\vec{r}_0, \omega)$  is a total electric field at the position of the probe molecule  $\vec{r}_0$ ,  $\omega$  is the frequency and  $\vec{E}_0(\vec{r}_0, \omega)$  is the strength of the incident field.

Firstly, COMSOL Multiphysics software was employed to calculate the absorption cross-section (ACS) and the SERS EF of the probe molecule near an isolated MXene flake, either in a solution, or on a substrate. Throughout the paper, in several simulations we used the dielectric function  $\epsilon_M(\omega)$  of  $\text{Ti}_3\text{C}_2\text{T}_x$ , measured in [5,15]. In COMSOL, to calculate accurately the EF, it is required to introduce the dielectric function of the dye molecule as well. In the Supporting Information (SI-2) we show that the R6G molecule in different media can be modelled as a small sphere possessing a macroscopic dielectric function  $\epsilon_R(\omega)$ . To obtain  $\epsilon_R(\omega)$  of a small sphere with radius  $R$ , as an auxiliary parameter, the imaginary part of polarizability  $\alpha_i(\lambda)$  of the dye molecule on glass substrate, or in aqueous solution, is extracted from experimental data of the absorption spectrum [34-36]. The real part of the dielectric function is calculated using the Kramers-Kronig relation [36, 37].  $\epsilon_R(\omega)$  is obtained according to the procedure described in (SI-2) and employed in all simulations.

MXene flakes were modeled as NPs of different geometries namely, nanoellipsoids (NE), nanorods (NR), and nanospheroids (NS) with longitudinal sizes up to  $2\mu\text{m}$ . We note that MXene flakes easily synthesized in many experiments have lateral sizes in the micrometer range [38]. In all our simulations the electric field of incident wave is oriented along the longest axis of NPs (in COMSOL we set it along X-axis) and the field propagates parallel to the shortest symmetry axis in case of NE (Z - axis) or transversal axes of NR and NS particles.

The resulting spectra for the ACS and the EF are accompanied with corresponding charge and near field distribution maps extracted at specific wavelengths. In all simulations the spatial distribution of electric field is normalized to the amplitude of the incident field. The distance

between the dye molecule and the surface of the NP embedded in water or on a glass substrate were also varied (starting from the shortest separation of  $s = 0.4\text{nm}$ ).

Below, in Figure1, we present the EF of SERS from R6G molecule near the apex of single oblate  $\text{Ti}_3\text{C}_2\text{T}_x$  MXene NE with the long axis  $2a = 500\text{nm}$  and aspect ratios  $\eta_1 \approx 3$  and  $\eta_2 \approx 15$  with  $\eta_1 = a/b$  and  $\eta_2 = a/c$ ,  $2b$  and  $2c$  are the short and shortest axes of the ellipsoid, respectively. This choice of geometrical parameters of the NE is determined by the need of describing the nanoparticle with approximate shape of synthesized MXene flakes always presenting sharp edges, leading to strong lightning-rod effect.

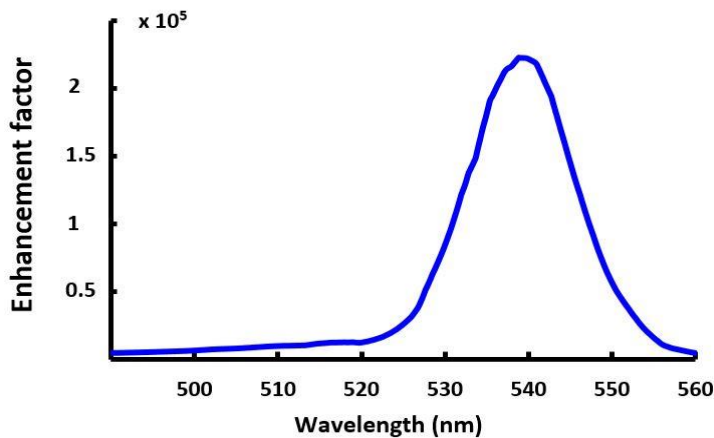


Figure1. EF of SERS from R6G molecule near the apex of single MXene NE with  $2a = 500\text{nm}$  and aspect ratios  $\eta_1 \approx 3$  and  $\eta_2 \approx 15$  on glass substrate. The distance from the apex of NE to the dye molecule, modeled as a small sphere of radius  $R = 0.31\text{nm}$  (see SI-2), is  $s = 0.4\text{nm}$ .

The EF maximum with value  $G \approx 2.21 \times 10^5$  achieved at the wavelength 545 nm, corresponds to the absorption peak of the dye molecule on glass substrate, [34]. The calculated EF value for the case of the dye molecule in water is  $G \approx 1.22 \cdot 10^5$  at 526 nm, which also corresponds to absorption peak of R6G, [36].

For a MXene NR with full length of  $l = 500\text{nm}$  and diameter of  $d \approx 170\text{nm}$  on glass substrate, we achieved the EF value of  $G \approx 2.29 \times 10^4$ . Thus, the EF for the NR is an order of magnitude smaller than for the NE. This difference is a consequence of larger radius of curvature of the apex of the NE comparing to NR, demonstrating the role of lightning-rod effect arising in sharp edges of NPs. We note that the presence of sharp edges in synthesized MXene flakes is evident in numerous scanning electron microscope (SEM) images (e.g. see [7]).

In order to understand the SERS enhancement mechanisms of molecules near MXene flakes, we use an example presented in Figure 2. It illustrates the dependence of ACS on wavelength for a NE with  $2a = 500\text{nm}$  and aspect ratios  $\eta_1 \approx 3$  and  $\eta_2 \approx 15$ .

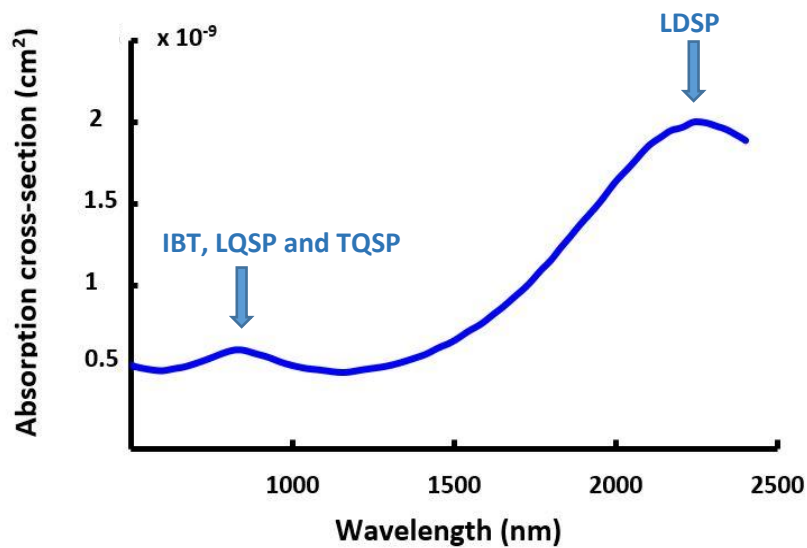


Figure 2. ACS dependence on wavelength in the system of spherical R6G molecule and MXene NE with  $2a = 500\text{nm}$  and aspect ratios  $\eta_1 \approx 3$  and  $\eta_2 \approx 15$ . The arrows indicate the positions of the longitudinal dipole surface plasmon resonance, interband transition, transverse and longitudinal quadrupole resonances.

From the ACS spectrum of Figure 2, we assume that the highest peak at  $\lambda = 2250\text{nm}$  corresponds to the longitudinal dipole surface plasmon (LDSP) resonance. To support this assumption, we carried out simulations for NEs of  $2a = 500\text{nm}$  but with other aspect ratios. The results revealed high sensitivity of the location of that peak to the shape of NP, which is a typical behavior of longitudinal dipole plasmon oscillations. The charge distribution map at  $\lambda = 2250\text{nm}$  corresponding to the dipole absorption peak is presented in SI-3. This sensitive to NP shape resonance was revealed also in high-resolution EELS experiments with  $\text{Ti}_3\text{C}_2\text{T}_x$  flakes [3, 39]. The same LDSP resonance at  $\lambda > 2200\text{nm}$  was revealed in [24] using UV-Vis-NIR absorption spectroscopy of micrometer sized  $\text{Ti}_3\text{C}_2\text{T}_x$  samples.

The smaller peak in the spectral range of  $\lambda = 500 - 1000\text{nm}$  of Figure 2. coincides with the maximum of absorption (or a dip in the transmittance spectrum) measured in  $\text{Ti}_3\text{C}_2\text{T}_x$  flakes in an aqueous solution, on a glass or sapphire substrates [5, 18, 22, 24, 40-42], as well as in measured EELS spectra [3, 39]. In optical absorption measurements, the maximum at around  $\lambda = 800\text{nm}$  was associated to IBT, which was theoretically verified in [18] (see SI in [18]). However, in [22, 40-42] the authors also hypothesized a possible excitation of SPs in the same spectral region, without specifying the type of collective oscillations. In [39] the peak at  $1.7\text{eV}(730\text{nm})$  found in the EELS spectrum of a  $\text{Ti}_3\text{C}_2\text{T}_x$  flake as well as the absorption resonance at  $\lambda = 785\text{nm}$  obtained in [26] for the same MXene were interpreted as a TDSP. In order to clarify these assumptions, the absorption spectrum of  $\text{Ti}_3\text{C}_2\text{T}_x$  flakes was studied theoretically in [17] and COMSOL simulations revealed the presence of LQSPs in the range  $\lambda \leq 1000\text{nm}$ . The physical origin of the peak in the spectral range of  $\lambda = 500 - 1000\text{nm}$  of Figure 2 becomes obvious by visualizing the surface charge and near-field maps of our COMSOL simulation. These maps for the NE of  $2a = 500\text{nm}$ ,  $\eta_1 \approx 3$

and  $\eta_2 \approx 15$  at  $\lambda = 540\text{nm}$  (corresponding to the EF maximum) are presented in the Figures 3 and 4 respectively.

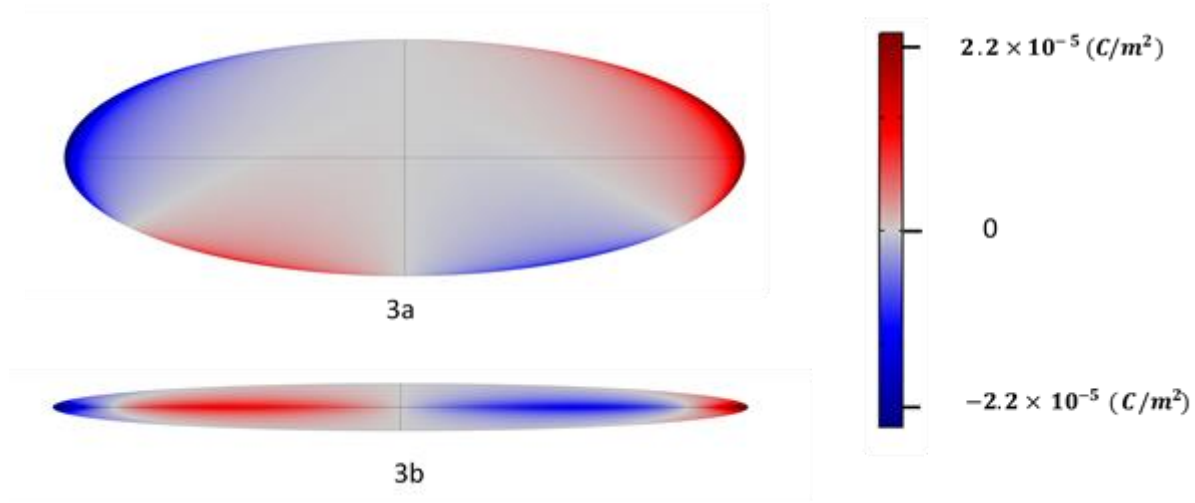


Figure 3. Surface charge distribution for a NE ( $2a = 500\text{nm}$ ) at  $\lambda = 540\text{nm}$  (view from the Y-axis (3a) and from the Z-axis (3b). Red and blue colors represent charges of opposite signs. The areas in gray correspond to zero charge.

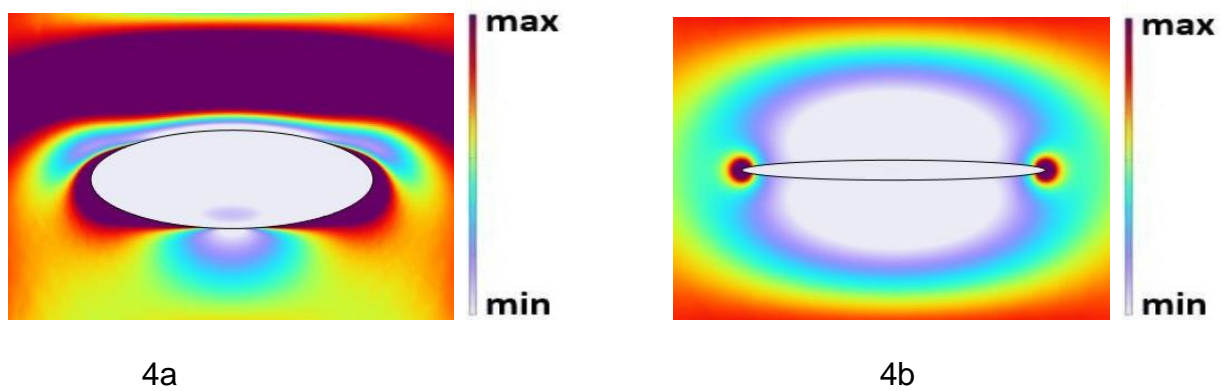


Figure 4. Maps of the near-field spatial distribution in NE ( $2a = 500\text{nm}$ ) at  $\lambda = 540\text{nm}$  in XZ-plane (4a) and XY-plane (4b).

Figures 3 and 4 clearly demonstrate quadrupole character of the SP oscillations. Whereas the LQSP in MXene at wavelengths  $\lambda \leq 1000\text{nm}$  were identified earlier [17], we see from Figure 3a what appears to be a TQSP oscillations in the surface charge distribution image. The transversal oscillations of the charge distribution in case of longitudinal polarization arise due to the inclined incidence of light wave to the surface of NE. Therefore, we conclude that at wavelengths  $\lambda \leq 1000\text{nm}$  LQSP and TQSP resonances both contribute to the absorption peak in Figure 2.

On the other hand, as above referred, in the spectral range  $\lambda = 500 - 800\text{nm}$ , COMSOL simulations for relatively small  $\text{Ti}_3\text{C}_2\text{T}_x$  NEs as well as for larger ones showed also a contribution of IBT to the absorption peak, for both longitudinal and transversal polarization of incident light [17, 18]. Thus, LQSP and TQSP resonances overlap with IBT. However, further investigation is necessary to understand their role in total enhancement of SERS. We want to stress that IBT can be the exclusive factor contributing to optical resonances, for relatively small NPs. We note that in MXene NPs with longitudinal size of  $2a < 500\text{nm}$ , quadrupole oscillations cannot be excited resonantly (see SI-4, where the dispersion of refractive index of MXene is discussed). Furthermore, considering that TDSPs in MXene appear at wavelength  $\lambda > 1130\text{nm}$  [5, 15] and LDSP resonance is located at much longer wavelength  $\lambda > 2000\text{nm}$ , we come to the important conclusion - in relatively small NPs only IBT resonances can be excited. It is this result that was obtained earlier (see Figure S7 b) of [18]) in simulations of absorption spectra of relatively small  $\text{Ti}_3\text{C}_2\text{T}_x$  MXene NEs (with  $2a < 300\text{nm}$ ) for transversal polarization. Indeed, as it is shown in the Supporting Information of reference [18], the wavelengths of resonances arising under excitation with transversal polarization are practically independent on the particle size. In particular, by varying the longitudinal size of a nanodisk from 10 nm to 300 nm, the position of absorption resonance around  $\lambda = 640\text{nm}$ , does not change, which is a direct indication of the contribution of

IBT as a source of these resonances. Thus, the material polarization in the wavelength range  $\lambda \leq 1000\text{nm}$  in Figures 3,4 is induced by quadrupole plasmons and IBT. It is relevant the fact that IBT can play a dual role in SERS, by enhancing the Raman signal directly and simultaneously exciting additional electrons to the conduction band increasing the flake polarization, induced by quadrupole plasmon oscillations.

The partial overlapping of LQSPs and IBT was confirmed by our simulations for other shapes of MXene flakes such as NSs and NRs of same length. It turns out that for wavelengths  $\lambda \leq 1000\text{nm}$  the ACS for different particle shapes has almost the same results as in Figure 2, which is typical for quadrupole plasmons and also for IBT [17]. The calculations show that peculiarities revealed for NEs appear also in NRs, however TQSPs in NR are less pronounced because of the larger radius of curvature compared to NE. The surface charge distribution and near-field map for a MXene NR, which confirm quadrupole character of oscillations, are presented in the Figures 5a and 5b.

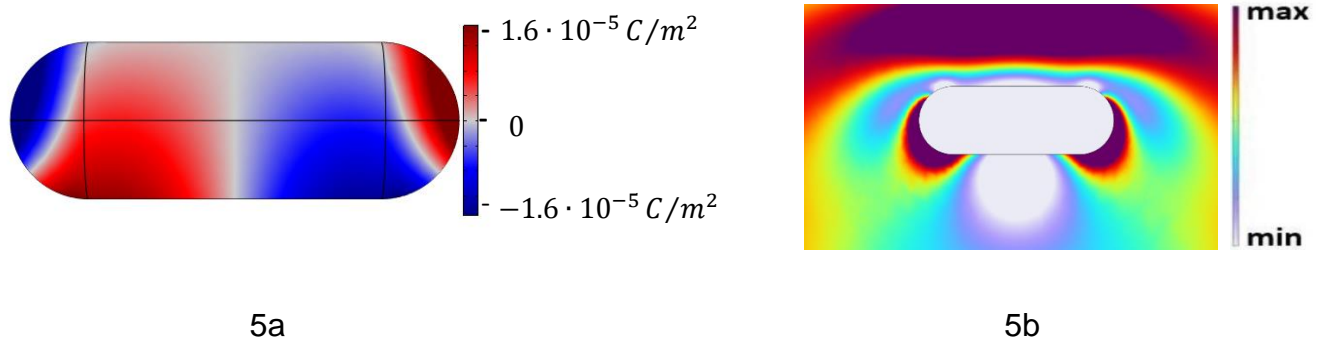


Figure 5. Maps of the surface charge distribution - glance along the Y-axis (5a) and near-field distribution at the XZ-plane (5b) in a NR (length -  $l = 500\text{nm}$  and diameter -  $d \approx 170\text{nm}$  at the resonance wavelength  $\lambda = 540\text{nm}$ ).

Obviously, an increase of the NP size leads to an increase in polarizability, and consequently increases the ACS. Moreover, simulations for larger particles demonstrate an increasing role of the quadrupole modes in absorption and correspondingly in near-field enhancement. For example, in Figure SI-4-1 we present the results of simulation of ACS and EF for the NE with  $2a = 1000\text{nm}$  on glass substrate and obtained a theoretical EF ) close to the value estimated in experiments [18, 20, 26]. Comparing Figures 1 and 2 with Figure SI-4-1 we see that larger particles provide more favorable conditions for exciting quadrupole plasmons, and consequently larger values of the ACS and SERS EF (see SI-5).

We note that the simulations were carried out for larger NRs with lengths of  $l = 1000\text{nm}$  and different diameter. The aforementioned characteristics in ACS and EF were also revealed for a NR of  $l = 1000\text{nm}$  (ACS and near-field enhancement curves are presented in Figure SI-4-2). In summary, in Figures SI-4-1,2 although the ACS of the NR is larger than that of NE, due to its bigger volume, the EF of NR turns out to be smaller. This is attributed to the smaller radius of curvature of the NE causing a stronger lightning-rod effect.

Simulations based on a further increase of size of ellipsoidal flakes ( $2a = 1500\text{nm}$  and  $2a = 2000\text{nm}$ ) does not lead to a significant change in the absorption spectrum in the visible-NIR range. In the spectral range of  $\lambda \leq 1000\text{nm}$  in NPs with aspect ratios  $\eta_1 \approx 3$ ,  $\eta_2 \approx 15$ , quadrupole and higher order SP mods start to play a more pronounced role in optical absorption processes (see e.g. charge distribution map of MXene NE with  $2a = 2000\text{nm}$  in Figure 6).

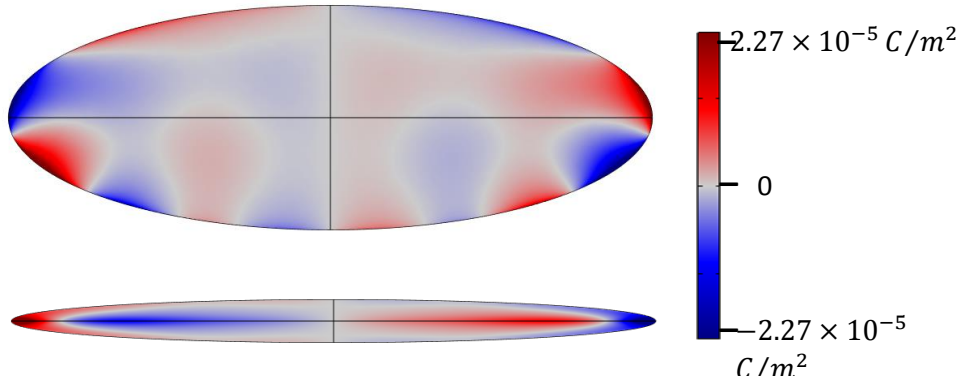


Figure 6. Surface charge distribution maps for NE ( $2a = 2000\text{nm}$ ) at  $\lambda = 540\text{nm}$  (glance along the Y-axis (7a) and Z-axis (7b)). Red and blue colors represent charges of opposite signs. The areas in gray correspond to zero charge.

We found that further increase of sizes of ellipsoidal flakes of  $2a = 1500\text{nm}$  and  $2a = 2000\text{nm}$  and aspect ratios  $\eta_1 \approx 3$ ,  $\eta_2 \approx 15$  does not lead to higher enhancement in the EF of Raman signal. For example, the EF value for  $2a = 2000\text{nm}$  ellipsoidal flake despite the larger volume is only  $2.4 \cdot 10^5$  whereas for  $2a = 1000\text{nm}$  NE with the same aspect ratio the EF is  $G = 2.7 \times 10^5$  (see SI-4-1b). The reason for this small change of the EF in large NPs (increase of only 10%) is directly connected with the radius of curvature at apex of NE which are  $R_1 = a/(2\eta_1^2)$  and  $R_2 = a/(2\eta_2^2)$ . Indeed, the increase in length of NE keeping constant the aspect ratios, causes an increase of  $R_1$  and  $R_2$ , therefore weakening lightning-rod effect. By keeping the particle volume constant and increasing the aspect ratios, a significant increase of the EF could be expected. To test this assumption, we have done simulations using NPs of different aspect ratios, but having the same volume, to assess the role of the sharpness of the NP in EF. NSs of equal volume but different shape as  $2a = 1000\text{nm}$  and  $2b = 400\text{nm}$ ,  $2a = 1500\text{nm}$  and  $2b = 327\text{nm}$ ,  $2a = 2000\text{nm}$  and  $2b = 280\text{nm}$ , give for the EFs the

following values  $G = 5.71 \times 10^4$ ,  $G = 1.12 \times 10^5$ , and  $G = 1.12 \times 10^5$ , respectively. Thus, isolated MXene substrates with realistic sizes and arbitrary shapes provide an EF of order of  $10^5$ .

Interestingly, in larger particles with  $2a = 1500\text{nm}$  and  $2a = 2000\text{nm}$  a new resonances appear in the ACS spectrum, as is shown in the Figure 7. For both NPs, the ACS has new maxima at wavelengths  $\lambda = 1540\text{nm}$  and  $\lambda = 1830\text{nm}$ . The corresponding surface charge distribution maps (see SI-6) clearly show that both a longitudinal and a transversal quadrupole modes contribute to these resonances. It is well known that quadrupole plasmons in nanoparticles are excited at wavelengths that approximate the particle size. In Figure SI-4, for a particles with length of  $1500\text{nm}$  and larger, this condition is satisfied. Thus, the new absorption peaks at long wavelengths in single NSs of micrometer size are due to the hybridization of longitudinal and transversal plasmon oscillations. We must note that this effect was also found for MXene dimers of smaller size, where coupling of different plasmon modes takes place in interacting NPs [17].

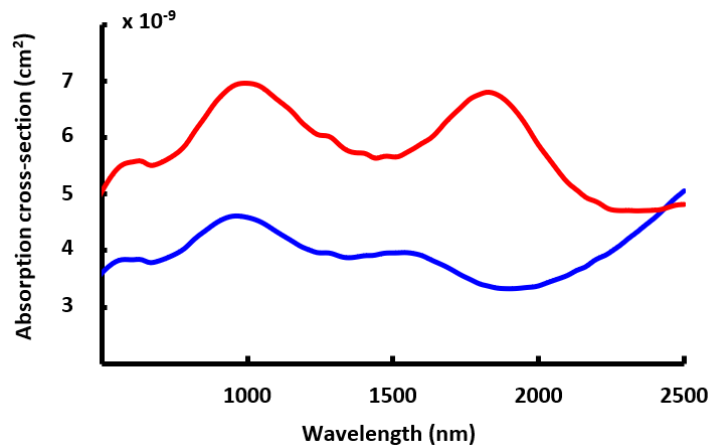


Figure 7. ACS dependence on wavelength in the MXene NE with  $2a = 1500\text{nm}$  (blue) and  $2a = 2000\text{nm}$  (red) (aspect ratios  $\eta_1 \approx 3$  and  $\eta_2 \approx 15$ ).

In summary, the EF from R6G on MXene substrates of micrometer sizes weakly depends on geometry of NPs. The reason of such behavior is that in absence of strong dipole SP oscillations in vis-NIR range Raman signal comes from IBT and quadrupole plasmon resonances.

## **2. Hot spot effect in coupled $Ti_3C_2T_x$ flakes as SERS Substrate**

Atomic force microscopy (AFM) images of MXene flakes show often bent sheets and curved surfaces with a number of edges supporting the origin of localized strong EM fields. Consequently, MXene flakes deposited on substrate or in solution can provide favorable conditions for another EM mechanism of SERS – hot-spot effect. This is probably the reason for high values of EF reported (exceeding  $10^6$ ) in experiments with  $Ti_3C_2T_x$  substrates [18, 20, 23].

In this Section in order to investigate this effect, we use dimers of  $Ti_3C_2T_x$ , in a “end - to - end” configuration composed of identical NEs and NRs of different sizes on glass substrate with the R6G molecule located in the middle of the gap. In Figures 8 (a) and 8 (b) are presented the ACS and EF for a dimer of identical ellipsoidal particles of  $2a = 1000\text{nm}$  and aspect ratios  $\eta_1 \approx 3$  and  $\eta_2 \approx 15$  on the glass substrate. Comparing to the ACS of Figure 7a) the ACS of the dimer with  $2a = 1000\text{nm}$  is about twice as large for the NP with the same value of the longitudinal axis. The corresponding near-field and surface charge distribution images, showing patterns typical of quadrupole resonances are presented in Figure SI-6.

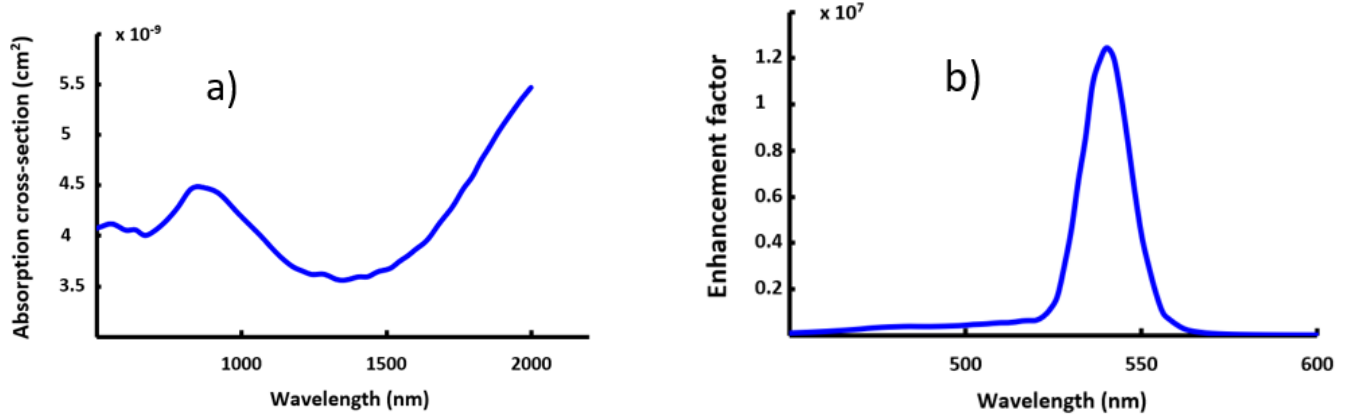


Figure 8. ACS (a) and EF (b) of the MXene NEs dimer on glass substrate with  $2a = 1000\text{nm}$  and aspect ratios  $\eta_1 \approx 3$  and  $\eta_2 \approx 15$ , The distance from the apex of each NEs to the dye molecule is  $s = 0.4\text{nm}$ . The incident EM field is polarized along long symmetry axis of the ellipsoids.

The EF for dimer (Figure 8 (b)) due to near-field coupling resulting in hot-spot effect is  $G = 1.2 \times 10^7$ . A notable contribution to the EF in the dimer is due to polarization induced by the absorption of the R6G dye at short wavelength (see Figure 8 (a)) at  $\lambda = 545\text{nm}$  [34].

Our simulations for dimers based on NRs with longitudinal size of  $\sim 1\mu\text{m}$  show that in all cases the ACS increases due to larger particle volumes comparing to dimers of NE, however the EF is smaller because of smaller apex sharpness. For example, for the NR dimer (length and diameter of each rod was  $l = 1000\text{nm}$  and  $d = 330\text{nm}$ ) the peak value of the EF was  $G = 9.1 \times 10^5$  indicating that the hot-spot effect dose not enhance substantially the Raman signal because of the round termination of the particles.

We have also done simulations for dimers and dye molecules in water. Using data of [36] for other shapes of MXene NPs in water we obtain results close to those observed in [18, 26].

To assess the dependence of ACS on the gap length in a dimer we calculated the absorption spectra of identical NS particles with sizes  $2a = 1000\text{nm}$  and  $2b = 2c = 400\text{nm}$  in “end-to-end” configuration, with incident field parallel to the symmetry axis of the dimer ( Figure. 9). For wavelengths below  $1300\text{nm}$  the ACS of the dimer does not depend on the gap size (see Figure 9). The reason for this behavior is due to the weak interaction between two NSs in wavelength range of interest ( $\lambda \leq 1300\text{nm}$ ), because of the quadrupole mode evidenced in the surface charge distribution. This insensitivity to the gap length is an important advantage in the preparation of MXene flakes as SERS substrates, since there is no need in a strict control of lateral sizes of synthesized NPs.

The minimum in the ACS of Figure 9, at  $\lambda = 1440\text{nm}$  for a inter-particle gap size of  $1.5\text{nm}$  was interpreted in [17] as a dip due to a Fano resonance formed by coupling between TDSP and LQSP modes. We verify in Figure 9 that this dip vanishes with increasing dimer gap.

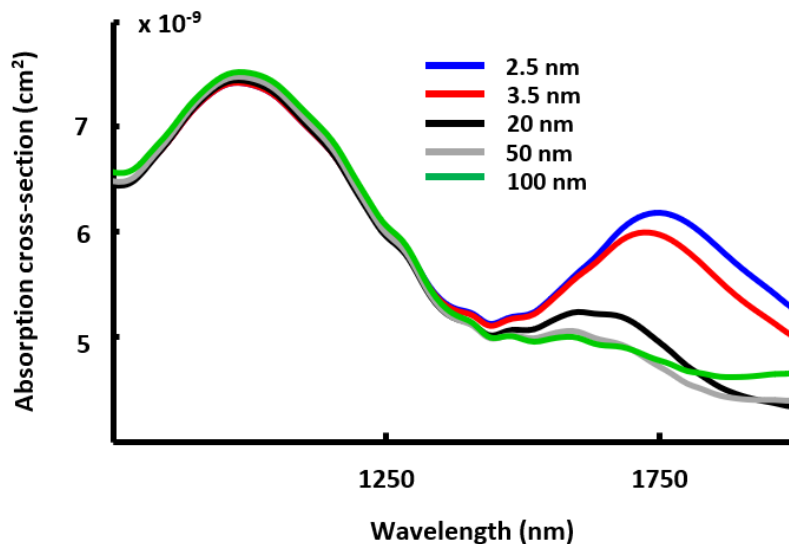


Figure 9. Dependence of ACS on the size of the gap of dimer composed of identical NSs with  $2a = 1000\text{nm}$  and  $2b = 2c = 400\text{nm}$  in “end-to-end” configuration when the incident electric field is parallel to particles longitudinal symmetry axis. The gap values are shown in the inset.

The surface charge distribution in a NS dimer at  $\lambda = 1440\text{nm}$  for a gap of  $2.5\text{nm}$  is presented in Figure 10. It shows the simultaneous excitation of a TDSP mode and a LQSP mode, which generate the destructive interference producing the Fano dip.

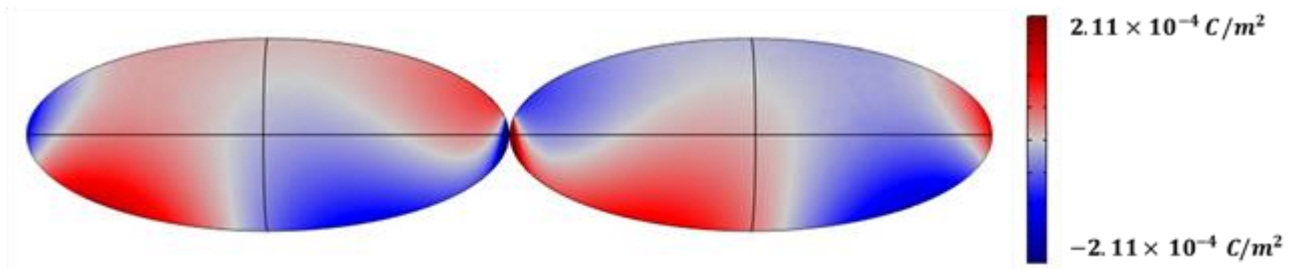


Figure 10. Surface charge distribution map in a NS dimer, for a gap of  $2.5\text{nm}$ , with  $2a = 1000\text{nm}$  and  $2b = 2c = 400\text{nm}$  at  $\lambda = 1440\text{nm}$ .

We note that the peak at longer wavelengths of Figure 9, contrarily to the peak at shorter wavelengths, corresponding to the excitation of the TDSP and the LQSPs strongly depend on the gap length. In conclusion, we must say that due to the hot-spot effect  $\text{Ti}_3\text{C}_2\text{T}_x$  flakes tightly placed on a glass substrate, or immersed in water can lead to rather high values of the EF.

## Discussion

It is demonstrated that together with IBT, LQSP and TQSP mods in MXene flakes contribute to the SERS enhancement for wavelengths below  $\lambda \leq 1000\text{nm}$ . Raman signal enhancement of the order of  $G = 10^5 - 10^7$  obtained in simulations of this article are determined by partial

overlapping of the IBT, LQSP, TQSP and R6G molecule absorption resonances, as well as by extra enhancement due to hot-spot effect. Unlike in dipole SP modes which are highly dependent on shape of NPs and generate large polarization in noble metals, all polarization mechanisms considered in this paper are much less sensitive to the shape of NPs. We conclude that although MXene substrates demonstrate moderate enhancements as compared to noble metal counterparts, nevertheless they can provide some advantages in conventional SERS applications. Despite the moderate enhancements the EF values are large and present a weak dependence on the particle shape and size.

In order to use the interaction of the dye in the EF we calculate a dielectric function of the R6G molecule based on experimental data of its ACS obtained in water or on glass substrate [34-36]. Since the dielectric function is a macroscopic property necessary to describe optical materials used in COMSOL, the R6G molecule is modeled as a small solid sphere of polarizability  $\alpha_{R6G}(\omega)$  equal to that measured for rhodamine molecule. This modelling was performed with the COMSOL simulation that allowed simple fitting procedure to choose proper radius of small sphere (see SI-2). Despite the fact that the polarizability is a tensor, usually the optical properties are averaged over a large number of R6G molecules random orientations. Thus, in experimental measurements the anisotropy of polarizability does not matter. For purpose of comparison with experimental data the same model was carried out when R6G molecule is placed near the MXene particle in vacuum.

Synthesized MXene flakes present a large variety of shapes, depending on the fabrication process. It is therefore, not possible to account for all the effects that may arise due to the various shapes present in samples of different experiments. Thus, we limit out theoretical analysis to the absorption experiments of MXene, for which we can model flakes of various shapes and assess the results obtained from experimental SERS measurements based on dye molecules. We study

MXene NPs with sizes matching those studied experimentally e.g. thin and thick samples, considering NPs of different shapes – NEs, NSs, and NRs.

In order to estimate the contribution of image effect into the EF value we calculated the electric field enhancement caused by MXene NE of  $2a = 500\text{nm}$  and  $2a = 1000\text{nm}$  in the absence of the dye molecule. The simulation show that the dependence of EF on the wavelength does not differ from those, presented in Figures 1 and SI-5-1, demonstrating the negligible role of image effect in SERS based on MXene flakes. The small contribution of image effect in this case is the result of absence of dipole SP resonance in the spectral range  $500\text{nm} - 1000\text{nm}$  considered. In principle, quadrupole SP resonances excited in the same spectral range may also contribute to the image effect. However, comparing to dipole SPs the electric field of quadrupole modes  $|\vec{E}|$ , decreases with  $r$  faster than  $r^{-3}$  ( $r$  is distance from NP to dye molecule). Therefore, in MXenes even at small separations the image effect does not cause significant enhancement of the Raman signal.

To identify separate contributions of different EM mechanisms causing SERS we also studied small MXene NPs with sizes much less than the wavelength by applying an analytical model based on quasistatic approximation (see SI-8). The EF of R6G molecule near the small  $\text{Ti}_3\text{C}_2\text{T}_x$  NS with semiaxes  $a = 30\text{nm}$  and  $b = c = 5\text{nm}$  for the separation of the molecule from the NS apex  $h = 0.565\text{nm}$  is presented in the Figure SI-7. Separate contributions into EF corresponding to the lightning rod and image effects in resonance condition are evident. From the simulations we verify that in the absorption spectrum of small MXene NPs there are no higher order multipole SP oscillations, since the role of inhomogeneity of the field at that spatial scale is negligible. Thus, higher order multipoles appear only in larger MXene NPs as it was demonstrated in the Sections 1 and 2.

## Conclusion

The dependence of the SERS EF from R6G molecule near titanium carbide MXene flakes of different size and shape is investigated theoretically in order to interpret results from experiments. In the numerical calculations of the EF the dye molecule is modeled as a small sphere with polarizability dependent on the wavelength of light, coinciding with the value found from the experiments. The calculations reveal a weak dependence of Raman EF on the shape and size of flakes for wavelengths  $\lambda \leq 1000\text{nm}$ , and identify a crucial role of quadrupole SP resonances in SERS with MXene substrates. The results of simulation for MXene substrates in vis-NIR spectral range provide EF values of the order of  $10^5 \div 10^7$  in agreement with experimental data for  $\text{Ti}_3\text{C}_2\text{T}_x$ .

The weak dependence of EF on linear sizes of easily synthesized and almost arbitrary shaped MXene NPs in visible-NIR range opens up new possibilities for using these substrates in conventional SERS applications.

**Funding:** The work was supported by the Science Committee of RA, in the frames of the research project Nr. 21T- 1C169.

## References

1. Naguib M.; Kurtoglu M.; Presser V.; Lu J.; Niu J.; Heon M.; Hultman L.; Gogotsi Y.; Barsoum M. W. *Adv. Mater.* **2011**, 23, 4248-4253. doi: 10.1002/adma.201102306.
2. Naguib, M.; Mashtalir, O.; Carle, J.; Presser, V.; Lu, J.; Hultman, L.; Gogotsi, Y.; Barsoum, M.W. *ACS Nano* **2012**, 6, 1322–1331.
3. Mauchamp, V.; Bugnet, M.; Bellido, E.P.; Botton, G.A.; Moreau, P.; Magne, D.; Naguib, M.; Cabioc'h, T.; Barsoum, M.W, *Physical Review B* **2014**, 89, 235428.
4. Magne, D.; Mauchamp, V.; Célérier, S.; Chartier, P.; Cabioc'h, T. *Physical Review B* **2015**, 91, 201409.
5. Dillon, A.D.; Ghidui, M.J.; Krick, A.L.; Griggs, J.; May, S.J.; Gogotsi, Y.; Barsoum, M.W.; Fafarman, A.T. *Advanced Functional Materials* **2016**, 26, 4162–4168.
6. Hantanasirisakul, K.; Zhao, M.-Q.; Urbankowski, P.; Halim, J.; Anasori, B.; Kota, S.; Ren, C. E.; Barsoum, M. W.; Gogotsi, Y. *Adv. Electron. Mater.* **2016**, 2, No. 1600050
7. *2D Metal Carbides and Nitrides (MXenes): Structure, Properties and Applications*, ed. by B. Anasori, Yu. Gogotsi, (Springer Nature, Switzerland AG, **2019**). doi:10.1007/978-3-030-19026-2.
8. Naguib, M.; Mochalin, V.N.; Barsoum, M.W.; Gogotsi, Y. *Advanced Materials* **2013**, 26, 992–1005.
9. Lukatskaya M.R.; Mashtalir O.; E. Ren C. E.; Dall'agnese Y.; Rozier P.; Taberna P. L.; Naguib M.; Simon P.; Barsoum M. W.; and Gogotsi Y. *Science* **2013**, 341, 1502-1505.
10. Simon, P.; Gogotsi, Y. *Nat. Mater.* **2020**, 19, 1151–1163.
11. Montazeri K.; Currie M.; Verger L.; Dianat P.; Barsoum M. W.; Nabet B. *Adv. Materials* **2019**, 31, 1903271.

12. Zhu, Z.; Zou, Y.; Hu, W.; Li, Y.; Gu, Y.; Cao, B.; Guo, N.; Wang, L.; Song, J.; Zhang, S.; Gu, H.; Zeng, H. *Adv. Functional Materials* **2016**, 26, 1793–1802.
13. Jhon, Y.I.; Koo, J.; Anasori, B.; Seo, M.; Lee, J.H.; Gogotsi, Y.; Jhon, Y.M. *Advanced Materials* **2017**, 29, 1702496.
14. Dong, Y.; Chertopalov, S.; Maleski, K.; Anasori, B.; Hu, L.; Bhattacharya, S.; Rao, A.M.; Gogotsi, Y.; Mochalin, V.N.; Podila R. *Advanced Materials* **2018**, 30, 1705714.
15. Chaudhuri, K.; Alhabeb, M.; Wang, Z.; Shalaev, V.M.; Gogotsi, Y.; Boltasseva, A. *ACS Photonics* **2018**, 5, 1115–1122.
16. E. Satheeshkumar, T. Makaryan, A. Melikyan, H. Minassian, Y. Gogotsi, M. Yoshimura, *Sci. Rep.* 6, 32049 (2016). Satheeshkumar, E.; Makaryan, T.; Melikyan, A.; Minassian, H.; Gogotsi, Y.; Yoshimura, M. *Scientific Reports* **2016**, 6, 32049.
17. Gonçalves M.; Melikyan A.; H. Minassian, Makaryan T.; Petrosyan P.; Sargsian T. *Photonics* **2021**, 8, 36.
18. Sarycheva, A.; Makaryan, T.; Maleski, K.; Satheeshkumar, E.; Melikyan, A.; Minassian, H.; Yoshimura, M.; Gogotsi, Y. *The Journal of Physical Chemistry C* **2017**, 121, 19983–19988.
19. B. Soundiraraju and B. K. George, *ACS Nano* **2017**, 11, 8892–8900.
20. Xie, X; Zhu, Y; Li, F; Zhou, X; & Xue, T, *Sci. China Technol. Sci.* **2019**, 62, 1202–1209
21. Wang, T.; Dong, P.; Zhu, Ch.; Gao, W.; Sha, P.; Wu, Y.; Wu, X. Lombardi, J.R.; Yang, Y. *Ceramics International* 47, **2021**, 30082-30090.
22. Sarycheva, A.; and Gogotsi, Y. *Chem. Mater.* **2020**, 32, 3480-3488
23. Ye, Y.T.; Yi, W.C.; Liu, W.; Zhou, Y.; Bai, J.; Li, F.; Xi, G.C. *Sci. China Mater.* 63, **2020**, 794 – 805.

24. Adomaviciute-Grabusove, S.; Ramanavicius, S.; Popov, A.; Šablinskas, V.; Gogotsi, O.; Ramanavicius, 9, **2021**, 223.
25. Peng, Y.; Lin, C.; Long, L.; Masaki, T.; Tang, M.; Yang, L.; Liu, J.; Huang, Zh.; Li, Zh.; Luo, X.; Nano-Micro Lett. 13,**2021**, 52.
26. Shevchuk, K., Sarycheva, A. & Gogotsi, Y. MRS Bulletin 47, **2022**, 545–554.
27. He, Z.; Rong, T.; Li, Y.; Ma, J.; Li, Q.; Wu, F.; Wang, Y.; Wang F. ACS Nano **2022**, 16, 4072–4083.
28. Chen, M.; Liu, D.; Du, X.; Lo, K.H.; Wang, S.; Zhou, B.; Pan, H.2D materials: Trends in Analytical Chemistry. **2020**, 130, 115983.
29. Moskovits, M. Reviews of modern physics **1985**, 57(3), 783.
30. Gersten, J; Nitzan, A. J. Chem. Phys. **1980**, 73, 3023-3037.
31. Liao, P. F.; & Wokaun, A. The Journal of Chemical Physics. **1982**,76(1), 751-752.
32. Metiu, H. Progress in Surface Science **1984**, 17(3-4), 153-320.
33. Xu, H.; Bjerneld E. J.; Käll M., & Börjesson, L. Phys. Rev. Lett. **1999**, 83(21), 4357-4360.
34. Itoh, T; Hashimoto, K.; Ikehata, A.; and Ozaki, Y. Appl. Phys. Lett. **2003**, 83, 5557:
35. Fang, Y; Blinn, K; Li, X; Weng, G; and Liu, M. Appl. Phys. Lett. **2013**, 102, 143112.
36. Djorović, A.; Meyer, M.; Darby, B.; and Le Ru, E. ACS Omega **2017**, 2, 1804–
37. Itoh, T.; Yuko, S.; Yamamoto, Y.; and Okamoto, T. J. Chem. Phys. **2020**, 152, 054710.
38. Alhabeb, M; Maleski, K; Anasori, B; Lelyukh, P; Clark, L; Sin, S; and Gogotsi, Y. Chem. Mater. 2017, 29, 7633–7644.
39. El-Demellawi, J.K.; Lopatin, S.; Yin, J.; Mohammed, O.F.; Alshareef, H.N. ACS Nano **2018**, 12, 8485–8493.

40. Lioi, D.; Stevenson, P.; Seymour, B.; Neher, G.; Schaller, R.; Gosztola, D.; Vaia, R.; Vernon, J.; and Kennedy, J. *ACS Appl. Nano Mater.* **2020**, 3, 10, 9604–9609.
41. Maleski, K.; Shuck, C.; Fafarman, A.; and Gogotsi, Y. *Adv. Optical Mater.* **2021**, 9, 2001563.
42. Colin-Ulloa, E.; Fitzgerald, A.; Montazeri, K.; Mann, J.; Natu, V.; Ngo, K.; Uzarski, J.; Michel W. Barsoum, M.; and Titova, L. *Adv. Mater.* **2023**, 35, 2208659 (1-10).